Journal of Materials Chemistry A

ROYAL SOCIETY OF CHEMISTRY

PAPER

View Article Online
View Journal | View Issue

Cite this: J. Mater. Chem. A, 2024, 12, 32191

Novel multi-functional sites in boron-based bi-atom catalysts synergistically boost C–C coupling for efficient CO electroreduction towards ethanol†

Huong T. D. Bui and Tore Brinck *

The electrochemical CO reduction reaction (CORR) is faced by challenges in achieving high-value-added C_2 products due to inefficient C–C bond formation and low selectivity. Using first-principles calculations, we propose a framework for boron-based bi-atom doping into a silicene monolayer (B–X@Si) to improve CORR catalytic efficiency. Transition metal (TM)-free B–B@Si and TM-containing B–Cu@Si serve as efficient bi-atom catalysts (BACs) with low limiting potentials (−0.28 and −0.63 V) and low activation barriers for C–C coupling (0.54 and 0.53 eV). The CO* binding strength of active sites with co-adsorbed CO* species follows the order TM < B < B–TM. Remarkably, the interplay within the B–TM pair strengthens CO* adsorption, driven by increased TM involvement, as characterized by the upward shift of the d-band center of TM in B–TM@Si relative to Fermi level. The coupling kinetics depend on the reactivity of C(CHO*) and CO* fragments within the decoupled CHO–CO* intermediate. Intriguingly, hetero-B–TM@Si systems display a trade-off between stronger CHO* and weaker CO* binding compared to the moderate binding observed in homo-B–B@Si. Among the TMs, Cu appears the most appropriate partner with B; the moderate synergistic effect of the B–Cu pair resulting in the smallest augmented C-affinity (CHO*) is offset by the weakest CO* binding strength on Cu itself, ensuring rapid C–C coupling similar to that of B–B@Si. Our BACs offer unique multi-functional active sites due to participation of host atoms (Si*) adjacent to the bi-dopants; these Si-atoms stabilize adsorbates, facilitate the subsequent C–C coupling step, and protect the C–O bond for selective ethanol production. This study provides theoretical insights for the development of advanced BACs with novel multi-adsorbing sites and tailored charge redistribution that enhance CO-to-C_2 conversion.

Received 15th July 2024
Accepted 31st October 2024

DOI: 10.1039/d4ta04897k

rsc.li/materials-a

1. Introduction

The ever-increasing consumption of carbon-intensive fossil energy sources such as oil, coal and natural gas has led to the continuous increase in carbon dioxide (CO_2) in the atmosphere.[1,2] Electroreduction of CO_2 (CO_2RR) and CO (CORR) into fuels and chemical feedstocks has been regarded a promising strategy to reach the carbon neutrality target.[2,3] Nevertheless, the diversity of final products formed through complex multi-reaction pathways has unfortunately become a selectivity bottleneck. While numerous studies have successfully demonstrated efficient CO_2RR/CORR into low-value C_1 products,[4–7] progress in enhancing the selectivity towards higher energy density multi-carbon chemicals (C_{2+}), such as ethylene (C_2H_4) and ethanol (C_2H_5OH), has been limited. The lack of progress can be traced to a challenging catalytic mechanism with sluggish kinetics/high thermodynamic energy of the C–C coupling step, high complexity of the post C–C coupling stage, and hard-to-control formation of H_2/C_1 side products.[8] Notably, the formation of C_{2+} compounds, where both CO_2RR and CORR share a common CO* intermediate towards same products,[9–11] underscores the potential to improve catalytic performance of CORR more effectively than that of CO_2RR.[12,13] Therefore, it is paramount to rationalize design strategies and elucidate mechanistic insights to improve CORR efficiency towards C_2 products.

Cu-based materials have generally been considered as the most promising candidates for efficient catalysis of CO_2/CO to a wide array of carbon-containing products, but due to their low C_{2+} selectivity and high overpotential they have so far not been able to meet the commercial standards.[14,15] Recently, progress has been made in enhancing the catalytic performance of Cu-containing bimetallic electrocatalysts through the implementation of engineering strategies such as heteroatom doping[16–18] and alloying.[19,20] These approaches provide dual active sites that can assist the C–C coupling process and

Department of Chemistry, CBH, KTH Royal Institute of Technology, SE-100 44 Stockholm, Sweden. E-mail: tore@kth.se

† Electronic supplementary information (ESI) available: PDOS, pCOHP and charge density difference of B–Ni@Si and B–Co@Si, Bader/Löwdin/Mulliken charge variations of four bare BACs, optimized geometries of 2CO* and H* intermediates, OCH_2CH* analysis, bond lengths of four optimized BACs structures. See DOI: https://doi.org/10.1039/d4ta04897k

optimize surface binding energies of adsorbed species, and thereby control the selectivity. In particular, exceptional binding of CO* has been observed in systems such as PdCu atom pairs in Pd–Cu_3N,[16] ZnCu binary sites in Zn alloyed with Cu(211)[19] and at the PdCu interface of a PdCu bimetal alloy,[20] promoting the CO dimerization process and resulting in high C_2 product selectivity and activity.

Among the abovementioned dimeric active-site platforms, bi-atom catalysts (BACs) have emerged as cutting-edge hetero-catalysts that maximize atomic utilization efficiency and minimize usage of material, thus accelerating CO_2/CO-to-C_2 conversion. Recently, Xia *et al.*[21] reported that two adjacent Cu atoms (Cu–N_3 moiety) in a graphitic sheet promote C–C coupling for further C_2H_5OH formation with faradaic efficiency (FE) of ~81.9%, and Zhao *et al.*[22] demonstrated that MOF homometallic Cu–Cu and heterometallic Cu–Sn with the hexaaiminobenzene (HAB) ligand promote the production of C_2H_4 and C_2H_5OH, respectively. Theoretical studies have predicted that Cu_2 supported on a porous C_2N layer (Cu_2@C_2N)[23] and Cu–B atomic pair decorated graphitic carbon nitride (B–Cu@g-C_3N_4)[24] are promising electrocatalysts for C_2 production. Interestingly, several recent works have highlighted the superior performance of non-Cu-based BACs over their Cu-based counterparts, contributing to the development of high-performance CO_2RR/CORR-to-C_2 cathode catalysts.[25–27] For example, FeCo/Fe_2@C_2N prefers to form C_2H_4 whereas CuCo/Cu_2@C_2N is selective towards CH_4 formation,[25] and FeB@C_2N is anticipated to be more efficient for CO_2RR towards C_2 products than B–Cu@C_2N.[26]

Silicene (Si) is a member of 2D semi-metallic xene family that has complementary properties to the well-known graphene, as exemplified by its enhanced chemical reactivity resulting from lowered aromaticity.[28–32] Our recent study unveiled that the introduction of a single B into Si monolayer, here termed B@Si, enables CO chemisorption *via* a unique combination of σ donation (C to B) and π-backdonation (B to C).[33,34] Additionally, the initial hydrogenation step of CO* to create CHO* consumes significantly less energy due to the participation of a neighboring host atom (Si*) alongside the B dopant, favorably binding O and C, respectively, thereby stabilizing the CHO* adsorbate on the B–Si* moiety. However, one drawback of the single-atom catalysts, SACs, is their insufficient number of active sites to facilitate the local CO concentration necessary for the vital C–C coupling in the formation of C_2 products. To address this, we explore a scenario where one B atom is co-doped with an X atom (X: B or TM (Mn–Cu)) into the Si monolayer to construct BACs, denoted as B–X@Si. Our comprehensive investigation uncovers that both TM-free B–B@Si and TM-based B–Cu@Si exhibit superior catalytic performance with low limiting potentials of −0.28 and −0.63 V, respectively, predominantly generating ethanol. Notably, while B demonstrates moderate CO* binding strength, TM itself exhibits weaker binding. However, the synergy of the B–TM pair enhances CO* adsorption in proportion to the extent of TM involvement (Cu < Ni < Co), which is correlated with the closeness of the d-band center of TM to the Fermi level (E_F). Moreover, the stability of the CHO* segment within CHO–CO* on B–X@Si, which is similar to that observed on single B@Si, renders the first reduction step of CO–CO* → CHO–CO* marginally endergonic. The subsequent kinetic favorability of CHO–CO* → OCHCO* coupling on B–B@Si and B–Cu@Si with low activation barriers of 0.54 and 0.53 eV, respectively, stems from the high reactivity of the C(CHO*) and CO* fragments of the decoupled CHO–CO* intermediate. The presence of TM in hetero-B–TM@Si regulates the electronic configuration of the B–TM pair, and fine-tunes the binding strength of adsorbed species involved in the coupling process. Moreover, host substrate atoms (Si*) serve as crucial active sites for stabilizing adsorbates that aid the initial C–C coupling and steer the post C–C coupling towards ethanol rather than ethylene. These findings not only shed light on the mechanism behind the pivotal C–C coupling process but also provide guidance for extending the concept of BACs with unique multi-active sites for the enhancement of CORR towards a single C_2 product.

2. Computational methods

Spin-polarized density functional theory (DFT) calculations were performed using VASP[35–37] with the Perdew–Burke–Ernzerhof (PBE) exchange–correlation functional[38] and projector augmented wave (PAW) potentials[39,40] for the treatment of core electrons. An energy cutoff was set to be 500 eV. DFT-D3 by Grimme was used to describe the long-range van der Waals (vdW) interactions.[41] The convergence criteria for force and electronic structure iterations were 0.02 eV $Å^{-1}$ and 1×10^{-5} eV, respectively. The *k*-point in Brillouin zone was sampled with a 3 × 3 × 1 Monkhorst–Pack grid. The vacuum space in the *z* direction was set to 20 Å for all structure models. Solvation effects were included by using the implicit solvation model implemented in VASPsol.[42] Bader charge analysis was deployed to compute charge population.[43] The projected Crystal Orbital Hamilton Populations (pCOHP) calculations, Löwdin and Mulliken charge analyses were analyzed by the LOBSTER package.[44] Vaspkit was used for data post-processing of PDOS.[45] *Ab initio* Molecular dynamics (AIMD) simulation was conducted under the NVT ensemble at 500 K with a 2 fs time step to evaluate the thermal stability of the structures.[46] Transition states searches and energy barriers were carried out using the climbing image nudged elastic band (CI-NEB) method.[47] Heyd–Scuseria–Ernzerhof hybrid functional (HSE06)[48] was used to analyze the electronic structures of selected structures, investigating the accuracy of the PBE functional for these types of systems. Further calculational details are given in the ESI.†

3. Results and discussion

3.1 Structure and stability

The pristine silicene model is designed and optimized in a stable two-dimensional low-buckled honeycomb configuration, featuring Si atoms in sp^2–sp^3 hybridization state (Fig. S1†). The calculated lattice constant (3.87 Å), buckling height (0.44 Å), interatomic Si–Si distance (or Si–Si bond length, d_{Si-Si} = 2.28 Å) align well with previous studies.[49–51] Two dopants, boron (B) and X, are deliberately placed into the double vacancy 5 × 5 Si

supercell lattice, termed as B–X@Si, consisting of 48 Si atoms and 2 dopants, as illustrated in Fig. 1a. A homogeneous B–B@Si structure is built where the second dopant X is also B, while heterogeneous B–TM@Si structures are constructed where X represents one of the five first-row non-precious transition metals (TM: Mn, Fe, Co, Ni and Cu). The stability of the six BACs is initially examined based on their formation energies (E_{form}) (Fig. 1b). Most structures display negative E_{form} values, indicative of their thermodynamic favorability, except for B–Fe@Si. We then calculate the dissolution potentials (U_{diss}) of TM in single B-embedded silicene (B@Si) to assess the electrochemical stability of these metal-based catalysts. The U_{diss} values tend to become more positive with an increase in the atomic number of TM. As such, both B–Mn@Si and B–Fe@Si with negative U_{diss} values appear unstable in electrochemical environment. Therefore, three hetero-BACs (B–Co@Si, B–Ni@Si and B–Cu@Si) along with the homo-B–B@Si structure are selected for our further CORR investigation.

In terms of atomic structure, the Si monolayer maintains its buckled honeycomb configuration after doping. While the introduction of two B substituents creates a nearly planar conformation in the vicinity of dopant sites in homo-B–B@Si, the TM dopants in hetero-B–TM@Si slightly protrudes out of the host substrate. The bond lengths between two dopants (d_{B-X}), or between a dopant and its nearest surrounding host atom (Si*) (d_{B-Si*}/d_{X-Si*}), as detailed in Table S1,† are in good accordance with the sum of their respective covalent radii, indicating strong covalent bonds.

The structural stability of our BACs is further scrutinized through electronic structure calculations and chemical bonding analysis (Fig. 1c and S2†). Differential charge density analysis unveils substantial electron density accumulation at the bonds between X and adjacent substrate Si* atoms, as well as in the proximity of X, consistent with the Löwdin charge analysis (Fig. S3†). To be more specific, a significant amount of electrons is transferred from Si* atoms towards X, with the B dopant accepting a much more negative charge than its TM partners in hetero-B–TM@Si. This charge transfer phenomenon can be attributed to the electronegativity order: B (2.04) > TM (Co – 1.88, Ni – 1.91 and Cu – 1.90) – Si (1.90). Moreover, partial density of state (PDOS) and projected crystal Hamilton population reveal pronounced PDOS overlaps between X and neighbour Si* atoms around the Fermi level (E_F), situated within bonding regions, verifying strong X–Si* bonds in the B–X@Si systems. Note that the interaction of B–Si* is stronger than that of TM–Si*, suggesting that the strong covalent bonds between non-metallic B and substrate Si* atoms primarily contribute to the high overall stability of the B–X@Si structure. More importantly, we observe a greater PDOS overlap between the two B atoms within homo-B–B@Si, visually signified by higher electron density concentrated in the B–B bond and quantitatively supported by a more negative integrated pCOHP (IpCOHP) value of the B–B bond, compared to that for B and TM within hetero-B–TM@Si, thus affirming the superior stability of the non-TM B–B@Si material over the B–TM@Si catalysts.

Intriguingly, hetero-B–TM@Si systems have a small portion of PDOS mixing between B and TM in the antibonding region across the E_F, with the degree of B–TM antibonding states following the order B–Cu < B–Ni < B–Co. This suggests a higher propensity for initiating and capturing CORR-adsorbed species, following the same trend.

We further perform MD simulations of our materials, taking B–B@Si and B–Cu@Si as examples, to examine their thermal stability. From Fig. 1d, both energy and temperature show slight

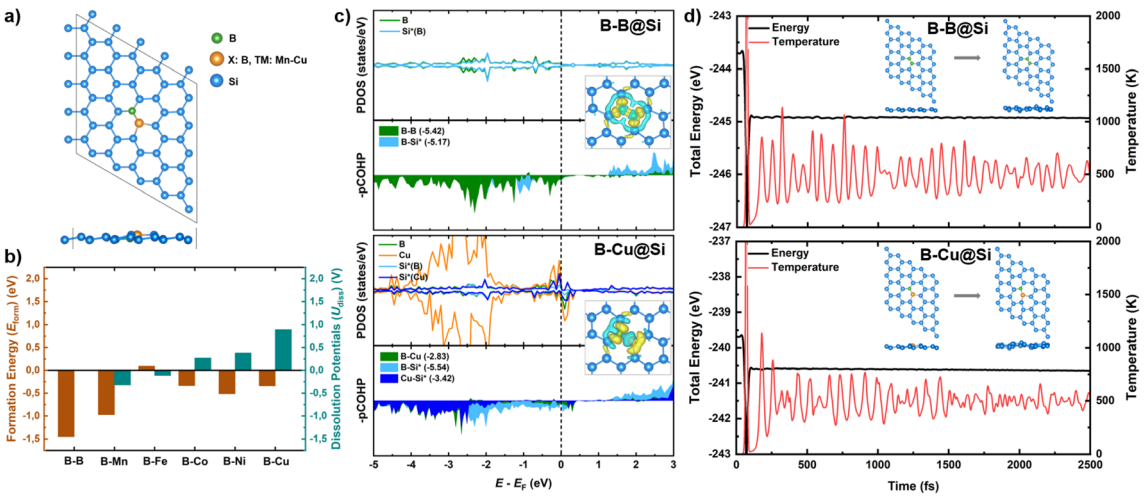

Fig. 1 (a) Designed models of B–X bi-atom doped into silicene (B–X@Si) from top and side views. (b) Formation energies (E_{form}) and dissolution potentials (U_{diss}) of transition metals (TM) in B-embedded silicene (B@Si). (c) Partial density of states (PDOS) of dopants (B/Cu) and one adjacent substrate atom (Si*); projected crystal orbital Hamilton population (pCOHP) of the dopant–dopant and dopant–host atom bonds, and corresponding integrated COHP (IpCOHP), taking homo-B–B@Si and hetero-B–Cu@Si as examples. The Fermi level displayed in dashed line is set to zero. Their corresponding charge density difference are also displayed. The isosurface value is 0.0025 e Å^{-3}, and the yellow (cyan) regions represent charge accumulation (depletion). (d) *Ab initio* molecular dynamics (AIMD) simulation of B–B@Si and B–Cu@Si at 500 K with the initial and final structures.

fluctuations over the simulation period at 500 K. Moreover, two adatoms still prefer to anchor at their favored sites in the defected Si substrate and no significant geometric distortion is observed. This stability originates from the strong covalent bonds between the two dopants and Si host atoms as well as between the two dopants themselves, confirming that the BACs are thermodynamically stable.

3.2 CORR *versus* HER

Hydrogen Evolution Reaction (HER), a primary side reaction during the CORR process, needs to be suppressed to increase FE of the CORR. Indeed, strong CO adsorption on the catalyst surface can hinder H from blocking active sites for CORR, thus minimizing the unexpected impact of HER on the CORR performance. Therefore, all possible configurations of H and two CO molecules adsorbed on four material surfaces were examined to identify the most stable one based on the lowest total energy (E_{total}), taking B–B@Si as an example, see Fig. S4.† For the first step of HER – the Volmer reaction, a proton tends to absorb on the bridge site of two dopants to form H* (Fig. S5†). Meanwhile, these dimers appear to act as favorable active sites for binding two CO molecules *via* upright chemisorption, which can serve as a key 2CO* intermediate and facilitate the C–C coupling step towards C_2 selectivity, as further discussed below. The adsorption energies of H* are less negative than the average ones of 2CO* in the four structures (E_{ads} [H*] > avg_E_{ads} [CO*]), indicating weaker adsorption of H^+ compared to CO (Fig. 2). These results suggest that H^+ is not likely to poison the catalytic surface; instead, the bi-doped active site thermodynamically prefers to be occupied by CO. Consequently, all four BACs exhibit a high selectivity preference for CORR over HER.

3.3 CORR activity and selectivity

3.3.1 Initial C–C coupling reaction. The formation of C–C bonds at the initial stage is widely acknowledged as a prerequisite for CO reduction to C_2 compounds, and three intermediates are of potential importance, *i.e.* CO*, CHO* and COH*.[52,53] Three principal pathways for C–C coupling are outlined in Fig. 3. The reaction free energy change (ΔG) for the direct dimerization of 2CO* to form coupled OCCO* intermediate is uphill for all BACs (shown in green line), ranging from 0.70 to 1.53 eV. Nonetheless, this coupling reaction on the four catalysts is energetically favored over that on the synthesized B-modified Cu(111) (1.60 eV).[54] The feasibility of the other two coupling pathways *via* CO* and its hydrogenated derivatives (CHO*/COH*) primarily relies on the preferred reduction of CO* into either CHO* or COH* on the confined B-anchored moiety. For these systems, CO* is more prone to reduction into CHO* than COH* due to the unique two-site adsorption mode, as will be discussed in detail later. As such, the initial reduction reaction of 2CO* to CHO–CO* is significantly less endergonic than that of COH–CO*. The subsequent coupling *via* CHPO–CO* to generate OCHCO* is energetically favored over that of COH–CO* to form HOCCO*, except for B–Co@Si. Remarkably, the CHO–CO* → OCHCO* coupling path for B–B@Si, B–Cu@Si, and B–Ni@Si, is significantly exergonic with ΔG values of −0.29, −0.65 and −0.20 eV, respectively, which are much lower values than that for Cu (211) (0.18 eV).[55] More importantly, Fig. S6† confirms that the formation of the OCHCO* intermediate towards the C_2 pathway is favored for the three BACs in comparison with the competitive C–H formation to create the decoupled counterparts (OCH_2–CO* or OCH–CHO*), which would be more likely to favor a C_1 pathway.

The kinetic energy barriers of this coupling on the three materials are calculated to be 0.54, 0.53 and 0.94 eV, respectively (refer to Fig. 4), which is in accord with the trend of the above reaction free energy changes. Note that B–B@Si and B–Cu@Si require less activation energy for CHO* coupled to CO* than Cu (211) (0.68 eV).[55] A coupling reaction step at room temperature with a kinetic barrier below 0.75 eV (corresponding to a TOF of 1 s^{-1}) is indicative of fast kinetics.[56] B–B@Si and B–Cu@Si are found to be promising candidates, thermodynamically and kinetically favoring the CO–CO* → CHO–CO* → OCHCO* coupling route.

3.3.2 Post C–C coupling process. Here follows a meticulous investigation into the intricate CORR mechanism towards C_2 products after the initial C–C bond formation. As previously noted, the two coupling paths CO–CO* and COH–CO* are less likely to be of importance because of their higher energy penalty compared to that of CHO–CO* and are therefore excluded from consideration. We evaluate all possible reaction intermediates along seven successive proton-coupled electron transfer steps of the coupled OCHCO* species and compute their corresponding free energies to deduce the most favorable CORR pathway, as depicted in Fig. 5.

The hydrogenation of the OCHCO* adsorbate on B–B@Si and B–Cu@Si yields OCH_2CO* rather than OCHCOH* due to its persistent strong binding frame *via* B–C and two O–Si* bonds. The OCH_2CO* is then protonated at the O* site to generate OCH_2COH* with negligible ΔG values. Subsequently, although the free energy level of the created OCH_2C* intermediate together with the dehydration on two structures is approximately equal (around −1.80 eV), the formation of OCH_2CHOH* on B–B@Si (−1.07 eV) is higher than on B–Cu@Si (−1.87 eV). In this regard, the OCH_2COH* is favorably hydrogenated to

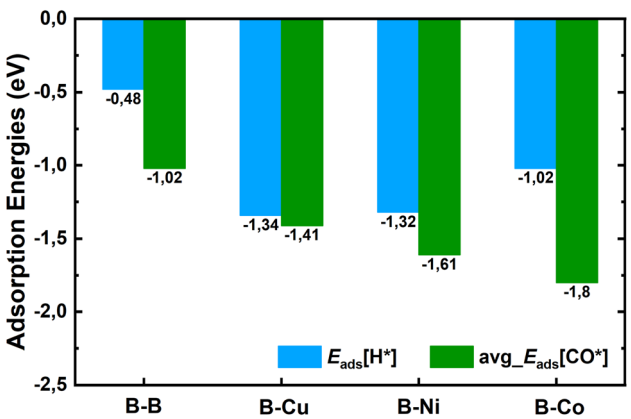

Fig. 2 Adsorption energies (E_{ads}) of H* and average 2CO* species on B–B@Si, B–Cu@Si, B–Ni@Si and B–Co@Si. Units: eV.

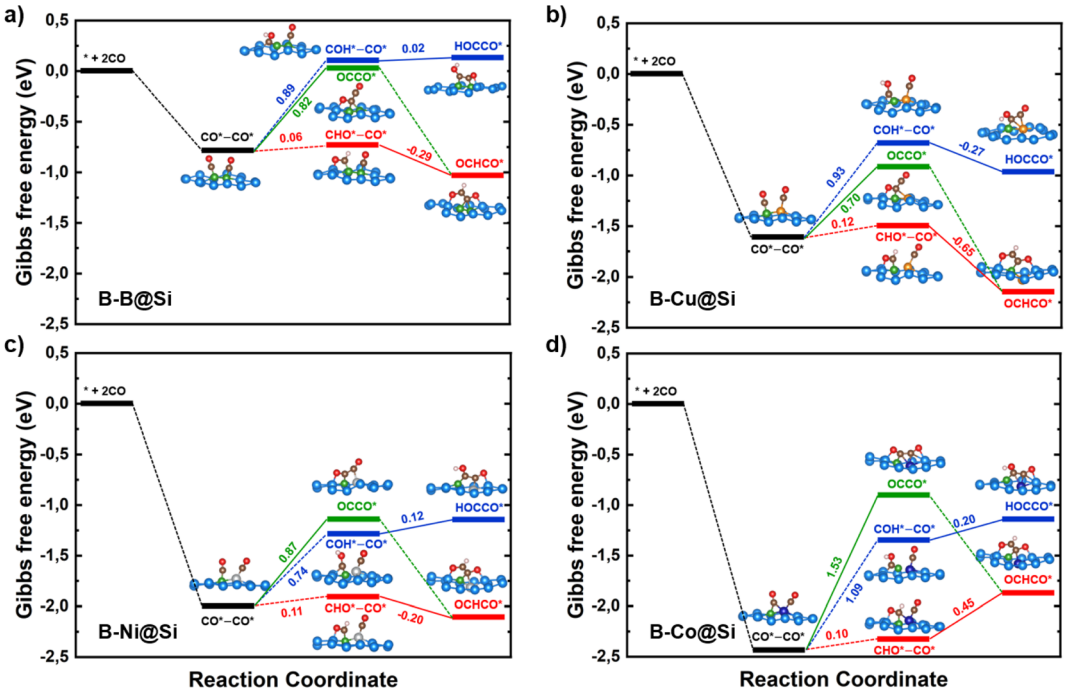

Fig. 3 Free energy profiles of different C–C coupling paths on (a) B–B@Si, (b) B–Cu@Si, (c) B–Ni@Si and (d) B–Co@Si at 0 V (*vs.* RHE). Inserts display the corresponding optimized structures of reaction intermediates and numbers show the corresponding reaction free energy change. The solid lines indicate the C–C coupling step. Color code: B – green, Cu – orange, Ni – silver, Co – dark blue, Si – light blue, C – brown, O – red and H – light pink.

produce OCH_2C^* + H_2O on B–B@Si and OCH_2CHOH^* on B–Cu@Si. The subsequent exergonic protonation step leads to the creation of OCH_2CH^*, a selectivity-determining intermediate, which bifurcates the pathway and determines the main C_2 product. That is, the subsequent hydrogenation of OCH_2CH^* may result in $HOCH_2CH^*$, $OCH_2CH_2^*$, or O* + C_2H_4. No C–O bond cleavage yielding C_2H_4 is observed after the protonation at $C(OCH_2CH^*)$ to form the stable $OCH_2CH_2^*$ species (see Fig. S7†). It is understandable that after the formation of the stable key coupled OCHCO* species, the host atom (Si*) with moderate oxygen affinity preserves the C–O bond well, implying a preference to produce CH_3CH_2OH over C_2H_4. Furthermore, the OCH_2^* part within OCH_2CO^* retains its binding backbone with Si* over a series of sequential reduction reactions. Consequently, the $OCH_2CH_2^*$ is more likely to be converted into $OCH_2CH_3^*$ than $HOCH_2CH_2^*$. It is predicted that both B–B@Si and B–Cu@Si undergo an endergonic reaction with a ΔG value of 0.28 and 0.59 eV, respectively; a proton attacks $O(OCH_2CH_3^*)$ to yield $HOCH_2CH_3$, which is considered the rate-determining step (RDS) of the entire CORR process. Noteworthily, although the two adsorbed species, OCH_2COH^* and OCH_2CH^*, exhibit analogous favorable interaction behaviors with B–B@Si and B–Cu@Si systems *via* O–Si* and C–(B–B)/C–(B–Cu), they show much stronger adsorption on B–Cu@Si than on B–B@Si, making the subsequent reduction steps on B–Cu@Si endergonic. This can be mainly explained by the fact that, as C in $OCH_2(C)OH^*$ and $OCH_2(C)H^*$ forms four bonds, the more weakly bound electrons in B–Cu (B–Cu@Si), as previously mentioned, are more likely to strongly bind with the C to form C–B and C–Cu bonds than in B–B@Si. In other words, the optimal electronic configuration in B–B@Si leads to moderate binding strength with CORR-adsorbed species in general,

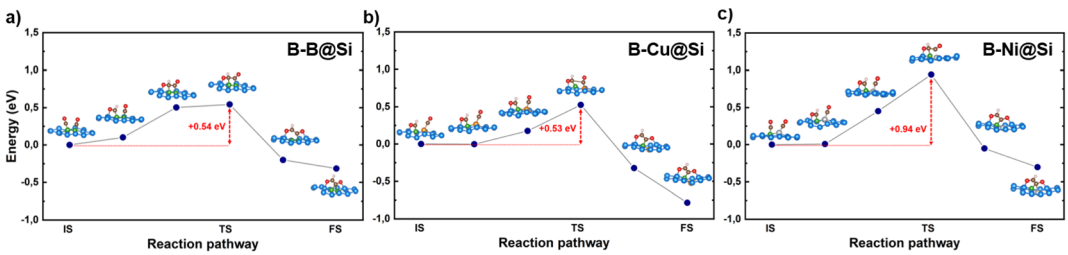

Fig. 4 The reaction path energy diagrams for the coupling step CHO–CO* → OCHCO* on (a) B–B@Si, (b) B–Cu@Si and (c) B–Ni@Si. The insets show the atomic structures of initial state (IS), transition state (TS) and final state (FS). Red numbers indicate the activation energy barriers. Color code: B – green, Cu – orange, Ni – silver, Si – light blue, C – brown, O – red and H – light pink.

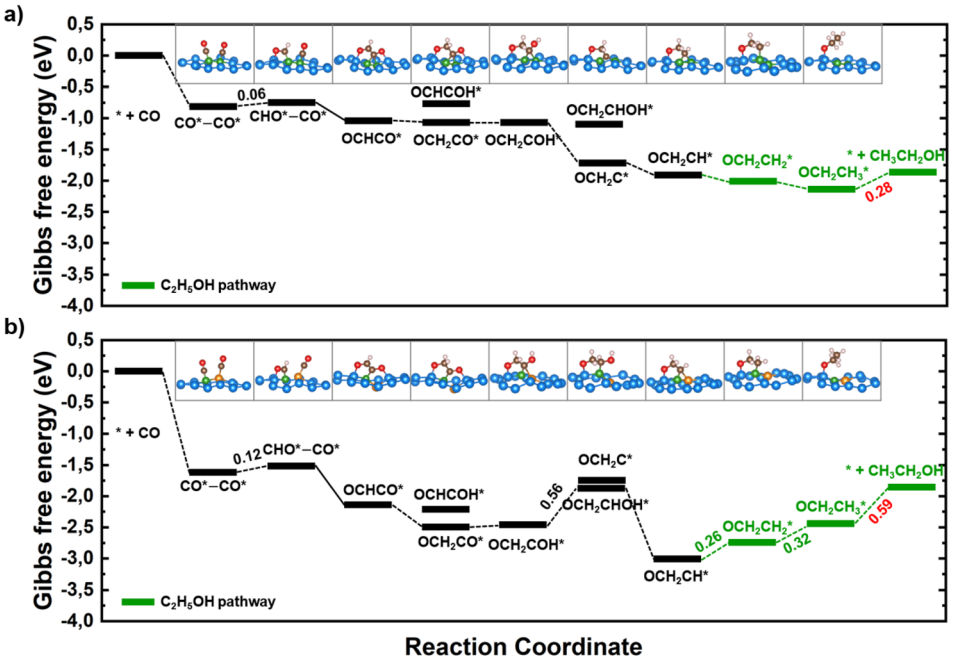

Fig. 5 Free-energy profiles for CO reduction on (a) B–B@Si and (b) B–Cu@Si. The potential determining step is labeled with the corresponding free energy change in red color. The green line demonstrates the best overall pathway towards CH_3CH_2OH. The insets show the lowest-energy optimized intermediate geometries along all the most thermodynamically CORR pathway. The solid lines indicate the C–C coupling step. Color code: B – green, Cu – orange, Si – light blue, C – brown, O – red, H – light pink.

resulting in slightly more favorable CORR performance on B–B@Si than on B–Cu@Si from a thermodynamic perspective.

The solvation effects on the electrochemical CO reduction of BACs are examined by comparing the Gibbs free energy diagrams generated using VaspSol with those in vacuum. Specifically, as shown in Fig. 3 and S8,† the energy required for the first crucial protonation step, CO–CO* → CHO–CO*, is slightly lower in the aqueous solution compared to the vacuum on B–B@Si (0.06 *vs.* 0.09 eV), B–Cu@Si (0.12 *vs.* 0.16 eV), B–Ni@Si (0.11 *vs.* 0.14 eV) and B–Co@Si (0.10 *vs.* 0.12 eV). Similarly, from Fig. 5 and S9,† the free energy change for the PDS ($OCH_2CH_3^* \rightarrow * + CH_2CH_3OH$) is reduced with VaspSol relative to that in vacuum for two potential catalysts, B–B@Si (0.28 *vs.* 0.36 eV) and B–Cu@Si (0.59 *vs.* 0.68 eV). These comparisons show that the aqueous environment has a slightly favorable effect on the CORR performance of our BACs.

3.4 Origin of the C–C coupling enhancement

3.4.1 CO co-adsorption and activation. The adsorption and activation of two CO molecules is of particular importance in dictating subsequent CO* hydrogenation and C–C coupling during the initial stages of CO-to-C_2 conversion. As shown in Fig. 6, two CO molecules chemisorb onto the dopant-pair sites of B–B@Si, B–Cu@Si, B–Ni@Si, and B–Co@Si, with negative adsorption energies (E_{ads} [2CO*]) of −2.04, −2.82, −3.21 and −3.59 eV, respectively. The CO* co-adsorption on BACs is thoroughly examined through an analysis of their structural/electronic properties and chemical bonding nature (Fig. 7). It is discerned that the B substituent in the four BACs, especially in homo-B–B@Si configuration, exhibits favorable binding with CO, characterized by bidirectional charge transfer between B and CO, as visualized by the charge density difference. The PDOS confirms a significant overlap between B and CO over energy windows below −6 eV and in proximity to the E_F, suggesting σ-donation from C to B and π-backdonation from B to C, respectively. This donor–acceptor behavior is consistent with our previous comprehensive study on single CO adsorption atop B in a single B@Si system that shows relatively analogous DOS overlap patterns of the B–CO interaction.[33] The interaction promotes CO adsorption and activates the CO molecule by

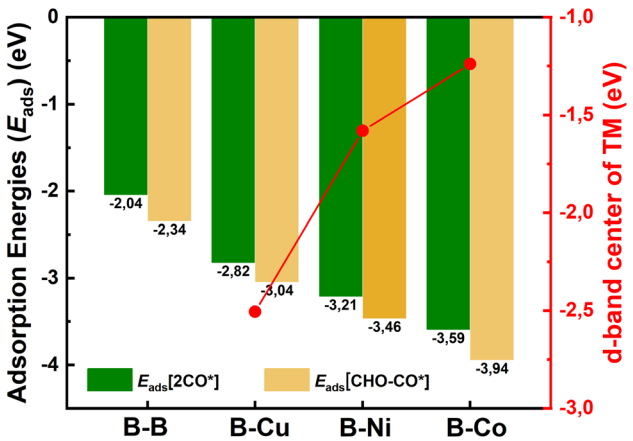

Fig. 6 Adsorption energies (E_{ads}) of 2CO* and CHO–CO* species on B–B@Si, B–Cu@Si, B–Ni@Si and B–Co@Si; and d-band centers of TM in bare hetero-B–TM@Si structures.

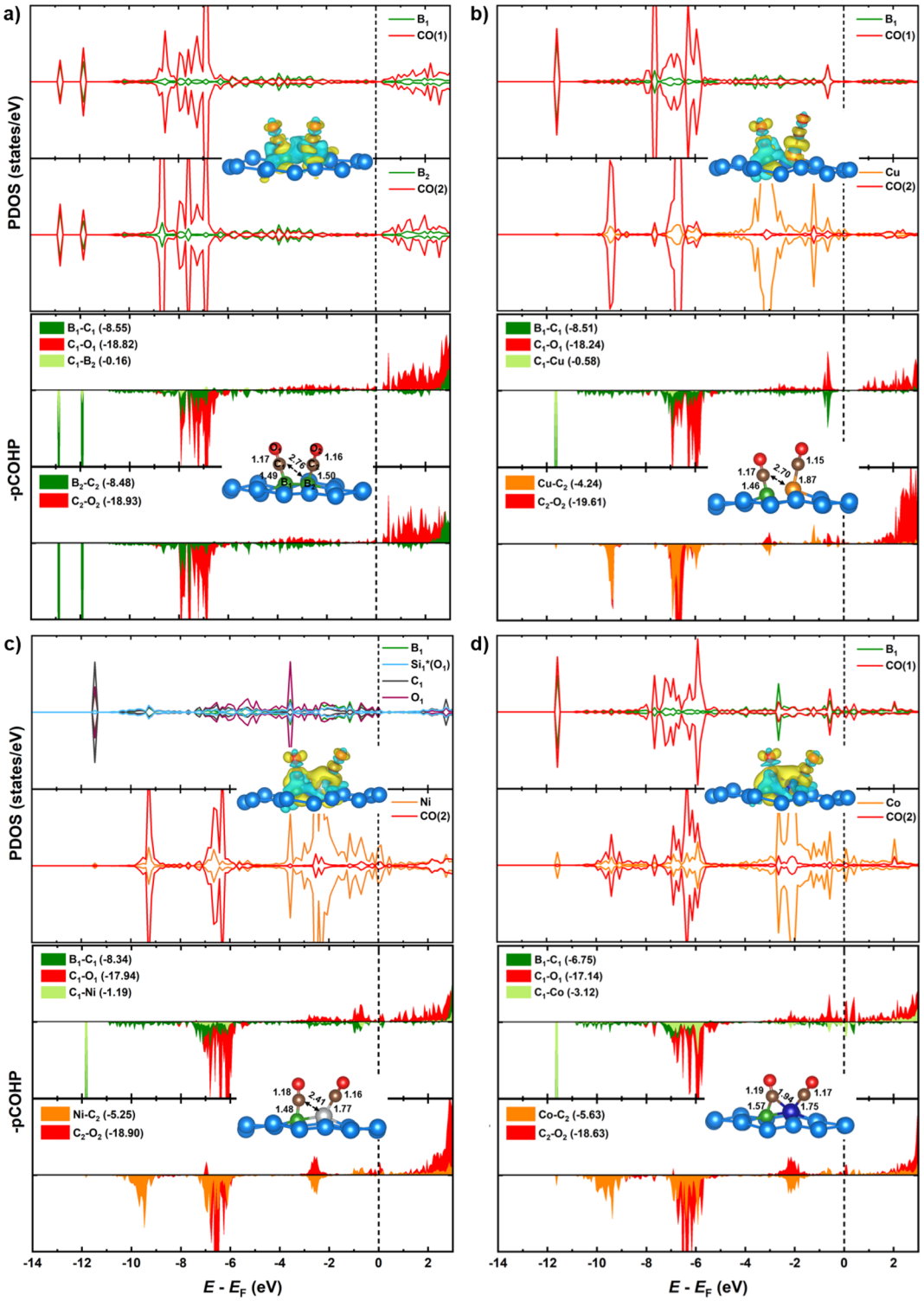

Fig. 7 Partial density of states (PDOS) of dopants and two adsorbed CO* species (upper panels) on (a) B–B@Si, (b) B–Cu@Si, (c) B–Ni@Si and (d) B–Co@Si. Their corresponding charge density difference are also displayed. The isosurface value is set to 0.0025 e Å^{-3}, and the yellow (cyan) regions represent charge accumulation (depletion). Projected crystal orbital Hamilton population (pCOHP) of the 2CO* intermediate. The Fermi level displayed in dashed line is set to zero. Their geometries with bond lengths are also displayed.

weakening the C–O triple bond, resulting in a longer C–O bond length (d_{C-O}) compared to that of the gas-phase CO molecule (1.14 Å).

Substituting the second B (B_2) with a TM in the homo-B–B@Si system reinforces CO* co-binding with the catalytic surface, with a strengthening trend as B–B@Si < B–Cu@Si < B–

Ni@Si < B–Co@Si. This strengthening can be attributed to the greater DOS contribution and denser charge clouds of TM (Cu < Ni < Co) together with the first dopant (B_1) for the pronounced interaction between dual active sites (B_1–TM) and the first CO molecule (CO(1)), leading to a combination of lengthened $d_{B1–C1}$ and shortened $d_{C1–TM}$ in 2CO*-adsorbed-B–TM@Si. Illustrated in pCOHP (lower panels), more populated bonding states of the C_1–TM bond (highlighted in light green), especially around E_F, follow the order of B–Cu@Si < B–Ni@Si < B–Co@Si, and this is quantitively verified by more negative IpCOHP (C_1–TM) values of −0.58, −1.19 and −3.12, respectively. This tendency aligns with the higher d-band center relative to the E_F of TM in B–TM@Si, *i.e.* −2.51 (Cu), −1.58 (Ni), and −1.24 eV (Co) (see Fig. 6), resulting in an increased binding affinity of active sites (B–Cu < B–Ni < B–Co) with CO(1) as well as (Cu < Ni < Co) with CO(2). Note that the involvement of B_2 (within homo-B–B@Si) in interacting with CO(1) is negligible (IpCOHP = −0.16), emphasizing the nearly independent roles of the two B in moderately binding with each CO molecule, in contrast to the hetero-B–TM@Si. In addition, the binding ability of TM (without B_1) with CO(2) is markedly weaker than that of TM–B_1 with CO(1) due to the PDOS of TM–C_2 interaction lying in the antibonding regions across the E_F (indicated by orange pCOHP curve), resulting in less negative IpCOHP values of TM–C_2 bond than the IpCOHP sum of B_1–C_1 and TM_1–C_1 bonds. Concurrently, the C–O triple bond in CO(2)* is less activated than that of CO(1)*, as reflected by the lesser elongation of $d_{C2–O2}$ and less negative IpCOHP (C_2–O_2) values. Clearly, the pCOHP shows more antibonding states of the C_1–O_1 bond around the E_F as the B–TM pair simultaneously interacts with CO(1), suggesting that CO(1) is more likely to be reduced than CO(2) further along the CORR process. The PDOS and pCOHP observations also verify the increasing binding strength of TM with CO(2) in the sequence of Cu < Ni < Co, which originates from a higher degree of DOS mixing in three energy ranges (−10 to −9 eV, −7 to −6 eV, and −3 to −2 eV) for the engagement in TM–C_2 bonding. In short, although the binding of CO(2)* on TM in hetero-B–TM@Si is weakened, the synergistic effect of the B–TM pair substantially enhances the binding of CO(1), thereby bolstering the overall stability of the co-adsorbed CO* intermediate, in comparison with the moderate binding of both CO(1) and CO(2) with homogeneous B–B@Si.

We have conducted hybrid functional calculations using the HSE06 functional and compare them with the PBE results to examine the sensitivity of the electronic structures of the 2CO*-adsorbed-B–X@Si system to the level of theory, as illustrated in Fig. S10.† Overall, the PDOS patterns with their corresponding bonding/antibonding states (depicted in pCOHP curves) are similar between two methods across the four systems; however, HSE06 shows a slight downward shift in the PDOS relative to E_F compared to PBE. This leads to slightly more negative IpCOHP values of all key bonds of the system when using HSE06, but the relative order of these IpCOHP values from HSE06 is consistent with the trend observed with PBE (see Table S2† for details). For instance, in the interaction with CO(1), while the engagement of B_2 in homo-B–B@Si remains minor with less negative IpCOHP values obtained by HSE06 (PBE in parentheses) of −0.20 (−0.16), the interplaying contribution of TM (Cu < Ni < Co) in hetero-B–TM@Si is more pronounced, with more negative IpCOHP values as follows: −0.67 (−0.58), −1.32 (−1.19) and −3.47 (−3.12). These comparisons validate the accuracy of the PBE functional used in our study to elucidate the mechanistic insights of CORR on our materials.

3.4.2 Preferential reduction over dimerization of co-adsorbed 2CO* species. As mentioned earlier, the dimerization of CO* and the first reduction into COH–CO* face high energy costs when beginning with two separate CO* entities. These unfavorable initial reaction steps arise from the strong binding affinity of 2CO* with bi-dopants, which is especially evident in B–Co@Si. This observation agrees with the Sabatier principle, which states that too strong CO adsorption on the catalytic surface can deactivate it for C–C bond formation and further reduction reactions. However, the initial protonation of 2CO* at CO*(1) to form CHO–CO* breaks this conventional linear relationship owing to the stable tetra-ring configuration of CHO* segment *via* two distinct bonds (B–C and O–Si*) (Fig. 8). The PDOS and the electron density difference also display a pronounced interaction between the B–Si* motif and CHO*, which is similar to the interaction observed in single B@Si,[33] in line with the favorable CHO* binding mode with our B–X@Si, while CO*(2) on X maintains its adsorption arrangement with minimal electronic alterations. Typically, the moderate CO*(1) and relatively strong CHO* adsorption on homo-B–B@Si leads to the exceptionally small ΔG value of 0.06 eV for this hydrogenation. Compared to the negligible influence of B_2 in homo-system, the trend of increasing TM involvement (Cu < Ni < Co) in the CHO* units is reflected by the more bonding states around the E_F (light green pCOHP curve) and corresponding more negative IpCOHP (C_1–TM and C_2–TM) quantities, which remains unchanged compared to the case of CO*(1) in the 2CO* intermediate. As a result, a slightly endergonic nature of the CO–CO* → CHO–CO* reaction is observed in hetero-systems, accompanied by a low energy demand of approximately 0.10 ∼ 0.12 eV.

3.4.3 Mechanistic insight into enhanced C–C bond formation. Considering the adsorption strength order of the decoupled CHO–CO* intermediate (Fig. 6), the subsequent coupling step to form OCHCO* is expected to occur with decreasing ease in the sequence: B–B@Si > B–Cu@Si > B–Ni@Si > B–Co@Si. However, the lower activation barrier for the CHO–CO* → OCHCO* reaction step results in an intriguing kinetic preference in the order B–B@Si ≈ B–Cu@Si > B–Ni@Si > B–Co@Si. To understand this exceptional trend, we first dissect the transformation in transition states of this coupling step on B–B@Si and B–Cu@Si (Fig. 4). CO*(2) tends to migrate towards the B site while C(CHO*) moves away from the surface to form a C–C bond, with its C_2 binding at the bridge site of B–X as well as its O_2 binding to the nearest positively charged host atom (Si_2^*). In this manner, the high reactivity of CO*(2) and C_1(CHO*) within the decoupled CHO–CO* intermediate is responsible for the coupling process. Because both CHO* and CO*(2) species are adsorbed on B dopants in the decoupled CHO–CO* intermediate with relatively moderate binding strengths, the homo-B–B@Si system favors the C–C bond

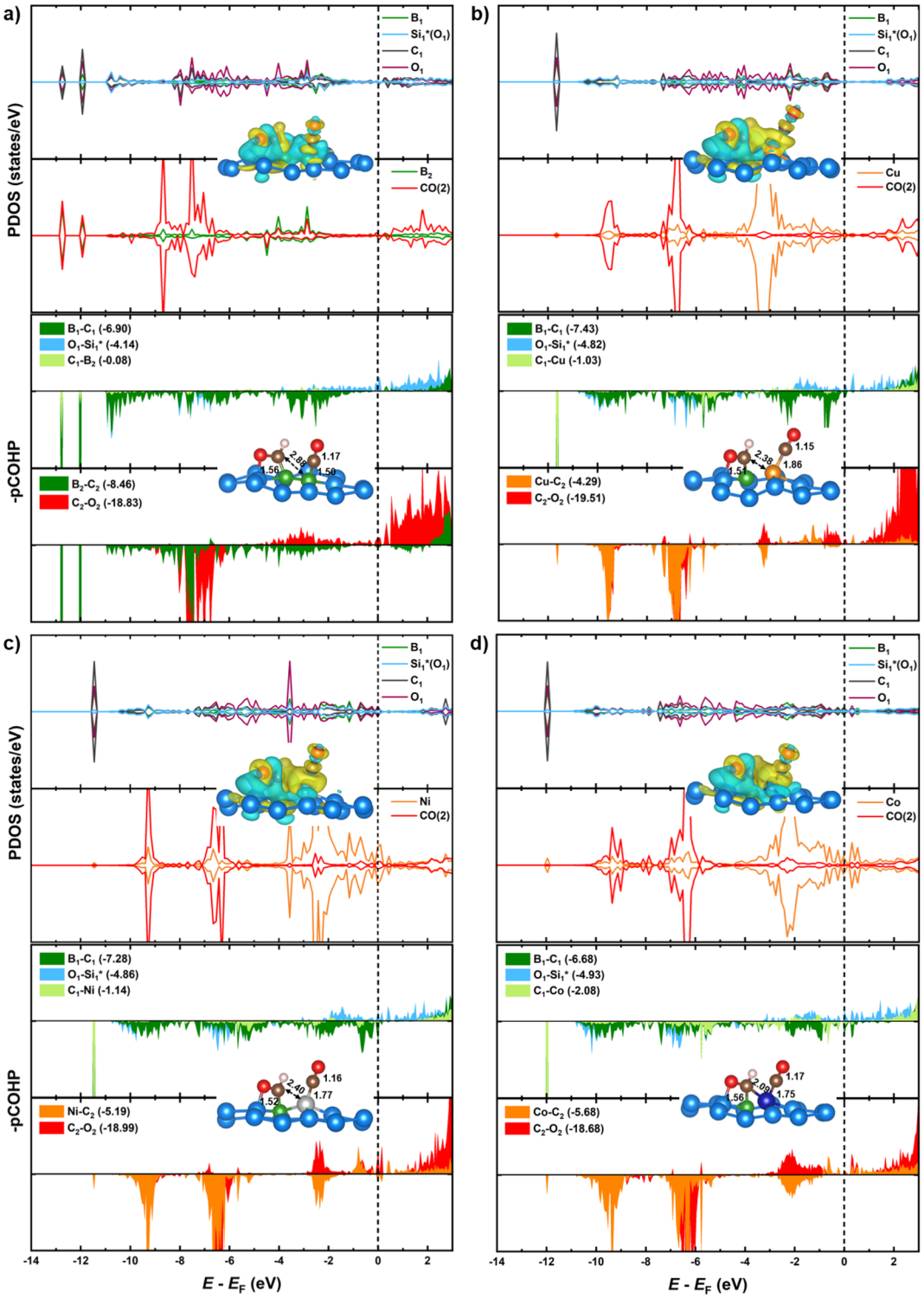

Fig. 8 Partial density of states (PDOS) of dopants, C and O atoms of CHO* part, and CO*(2) part (upper panels) on (a) B–B@Si, (b) B–Cu@Si, (c) B–Ni@Si and (d) B–Co@Si. Their corresponding charge density difference are also displayed. The isosurface value is set to 0.0025 e Å^{-3}, and the yellow (cyan) regions represent charge accumulation (depletion). Projected crystal orbital Hamilton population (pCOHP) of the decoupled CHO–CO* intermediate. The Fermi level displayed in dashed line is set to zero. Their geometries with bond lengths are also displayed.

formation. In the hetero-B–TM@Si system, the lower energy of the d-band center (Cu < Ni < Co) results in weaker interactions of CO*(2) and TM as well as C_1(CHO*) and hybrid bi-dopants (B_1–TM), as evidenced by less negative values of IpCOHP for TM–C_2 and C_1–TM, respectively (see lower panels in Fig. 8). It indicates that the higher reactivity of CO*(2) and C_1(CHO*),

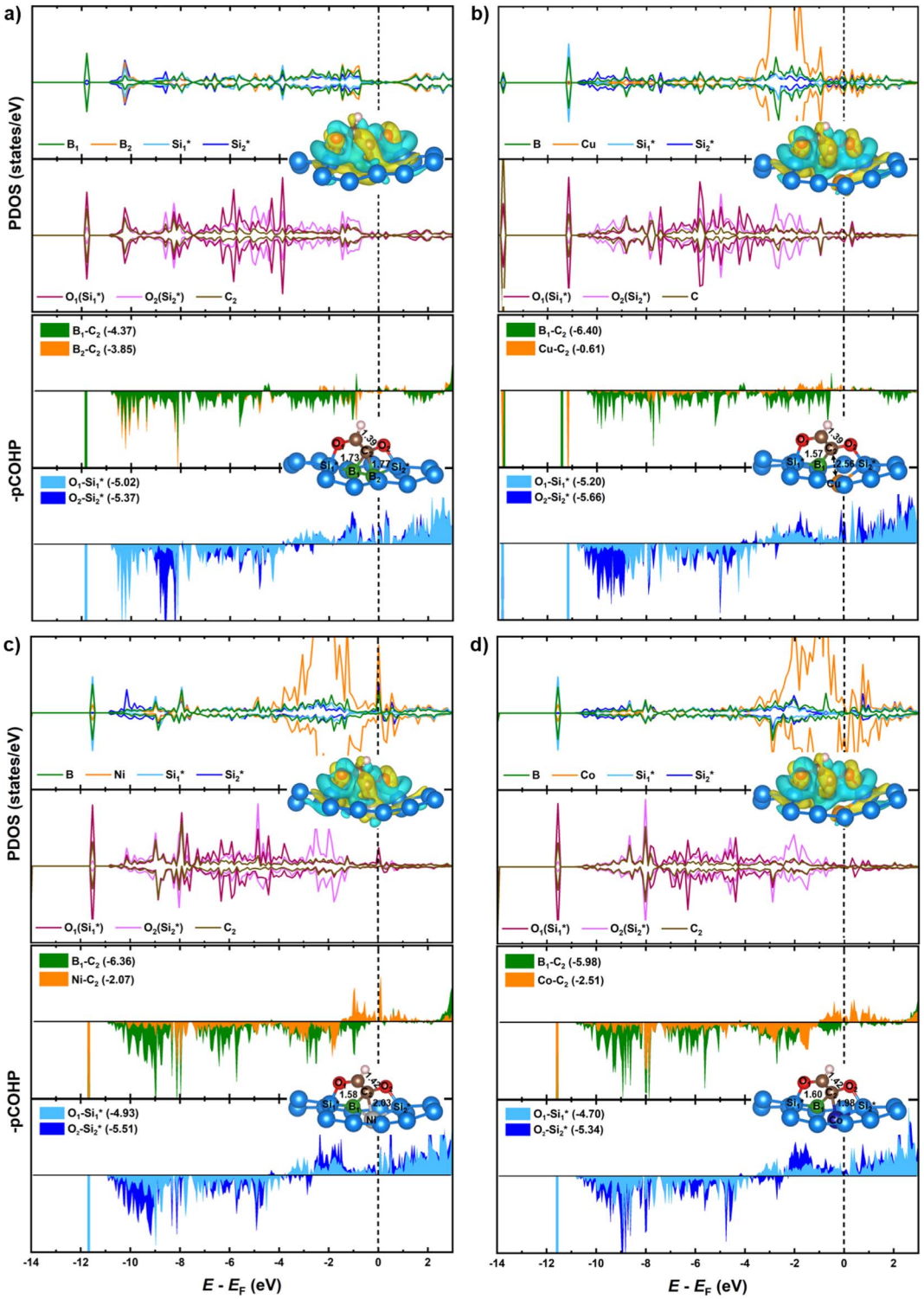

Fig. 9 Partial density of states (PDOS) of dopants, host atoms Si* (bonded to O), O_1 atom (OCH*), O_2 atom (CO*(2)), and C_2 atom (CO*(2)) (upper panels) on (a) B–B@Si, (b) B–Cu@Si, (c) B–Ni@Si and (d) B–Co@Si. Their corresponding charge density difference are also displayed. The iso-surface value is set to 0.0025 e Å^{-3}, and the yellow (cyan) regions represent charge accumulation (depletion). Projected crystal orbital Hamilton population (pCOHP) of the coupled OCHCO* intermediate. The Fermi level displayed in dashed line is set to zero. Their geometries with bond lengths are also displayed.

governed by the more moderate TM engagement, leads to favorable C–C coupling kinetics in the order of B–Cu@Si > B–Ni@Si > B–Co@Si. There is a trade-off between stronger CHO* and weaker CO*(2) adsorption on hetero-B–TM@Si compared to homo-B–B@Si. Notably, the moderate synergistic effect of B–Cu in the B–Cu@Si results in the slightest increase in its

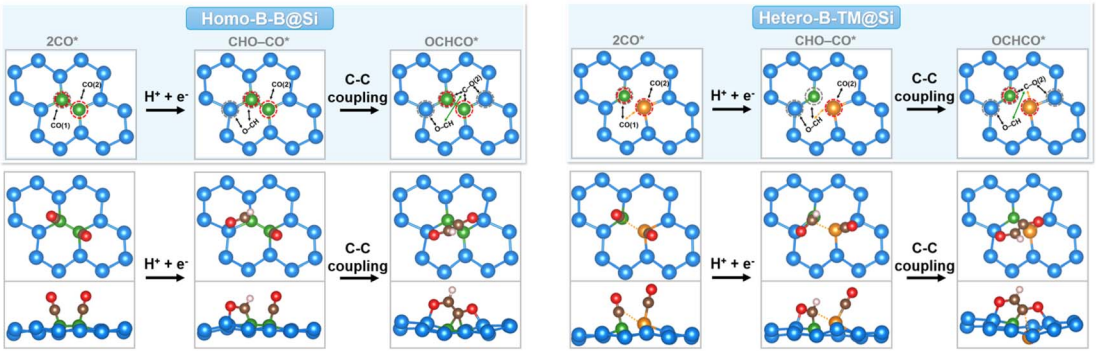

Scheme 1 Proposed scenarios of C–C coupling mechanism on B–X@Si (homogeneous B–B@Si and heterogeneous B–TM@Si). Taking the coupling process on B–B@Si and B–Cu@Si for examples with both top and side views of corresponding optimized intermediate geometries. Dark gray and red circles symbolize 'stabilize' and 'mobilize' functions of active sites. Green narrow displays C–C bond and orange dashed line indicates the TM involvement.

binding strength with CHO* and the weakest binding of Cu with CO*(2) among the three hetero-B–TM@Si systems; these features allow the B–Cu@Si to kinetically favor the CHO–CO* → OCHCO* coupling step, achieving similar performance to that of B–B@Si. We also calculated magnetic moments at the individual active sites (B and B/TM) for the CHO–CO* → OCHCO* reaction step to investigate the potential role of spin for the reactivity, see Table S3.† However, the magnetic moments of the two intermediates for the two best performing catalysts (B–B@Si and B–Cu@Si) are consistently zero. Thus, we conclude that magnetization is not a significant activity descriptor for these systems.

From Fig. 9, the main binding framework, consisting of one B_1–C_2 bond and two $O_1 - Si_1^*/O_2 - Si_2^*$ bonds, contributes to the stability of coupled OCHCO*. In fact, there is a substantial DOS overlap between B_1 and C_2 in the bonding region (green pCOHP) near the E_F with more negative IpCOHP (B_1–C_2) values. Notably, the C–C bond length of the OCHCO* adsorbate on all four structures ($d_{C1-C2} = 1.39 \sim 1.42$ Å) is shorter than the average of double and single C–C bond lengths ($d_{C-C} \approx 1.44$ Å), implying that the OCHCO* intermediate should be more stable as C_2 binds primarily to B_1. Indeed, a higher TM involvement (Cu < Ni < Co) in the TM–B pair within hetero-B–TM@Si for the interaction with C_2 weakens the stability of OCHCO*, resulting in significantly increased ΔG values for the coupling. Notably, the charge density difference indicates a low electron density between C_2 and Cu, accounting for the high stability of OCHCO*-adsorbed B–Cu@Si. Similarly, homo-B–B@Si, despite two B dopants sharing nearly equal moderate binding strength with C_2, exhibits less exergonic coupling than B–Cu@Si. Additionally, two positively charged substrate atoms (Si*) close to the two dopants preferentially bind with the negatively charged O*, as indicated by charge density distribution and relatively negative IpCOHP ($O_1 - Si_1^*$ and $O_2 - Si_2^*$ bonds). It is worth noting that the pCOHP curves of the O–Si* bonding fall into antibonding areas around the E_F, indicating that the Si* atoms haves moderately strong O affinity, reducing the likelihood of C–O bond scissoring in oxygen-bound intermediates such as OCHCO* or further OCH_2CO*. This preservation of the C–O bond may direct the CORR pathway bifurcation on our Si-based BACs towards C_2H_5OH rather than O* and C_2H_4, as discussed in Section 3.3.2.

The proposed C–C coupling mechanism of our homo/hetero-B–X@Si is summarized in Scheme 1 to provide an overview. First, two CO molecules vertically chemisorb with C pointing downwards at the dopant-pair sites. Each of the two B dopants in homo-B–B@Si independently binds one CO molecule with moderate binding strength. In hetero-B–TM@Si, the B–TM pair collaboratively strengthens the CO(1) adsorption (highlighted in orange dashed arrow), while the TM itself displays a relatively weak binding with CO(2). Next, CO(1)* is hydrogenated to form the stable adsorbed CHO* part *via* $O_1 - Si_1^*$ and B_1–C_1 in homo-B–B@Si or (B_1–TM)–C_1 in hetero-B–TM@Si, with similar TM contribution as in CO(1)* of the 2CO* intermediate. Then, within the decoupled CHO–CO*, CO(2)* with its inherent moderate-to-weak adsorption on X is more likely to shift towards B_1, concurrent with the movement of C(CHO*) out of the surface, leading to the formation of a C–C bond. Evidently, three main active centers, B_1 and two substrate neighbors (Si*), are responsible for stabilizing the adsorbed species involved in the C–C coupling process (highlighted in gray dashed circles). Furthermore, B_1 and X play a crucial role in regulating the reactivity of C(CHO*) for the C–C coupling (in red dashed circle). Indeed, when X is B, there seems to be no engagement of X in the moderate adsorption of CHO* on B_1, explaining the high mobility of C(CHO*). Conversely, if X is TM, a reduced TM contribution (Cu < Ni < Co) to the favorable C(CHO*) adsorption results in a more active C(CHO*). More importantly, X acts as a temporary active site to retain CO(2) before supplying it as a source for C–C coupling. In this manner, weaker CO(2)* adsorption is advantageous for boosting the migration of CO(2) towards the coupling.

4. Conclusion

In summary, we introduce a theoretical model of boron-based bi-atom doping into a silicene monolayer (B–X@Si) for CO reduction to C_2 end-products. Two bi-atom catalysts (BACs),

namely TM-free homo-B–B@Si and TM-containing hetero-B–Cu@Si, stand out as promising electrocatalysts with high thermodynamic stability, low limiting potentials of −0.28 and −0.63 V, respectively, and a high selectivity towards CORR over HER.

The B dopant serves as the preferred active site for CO capture and activation with its moderate binding strength *via* a noticeable "σ-donation – π-backdonation" pattern compared to its TM counterparts. The synergy between B and TM (B–TM) increases the adsorbed CO* stability through the greater degree of TM contribution, induced by the upward shift of the d-band center of TM towards E_F. The initial reduction of CO*-bound B (or B–TM) motifs within CO* co-adsorption on homo-B–B@Si (or hetero-B–TM@Si), respectively, requires significantly less energy owing to the unique CHO* binding mode with B (or B–TM) together with an adjacent host atom (Si*). Moreover, the combined high reactivity of C(CHO*) and CO* units within the decoupled CHO–CO* drives the CHO–CO* → OCHCO* coupling on B–B@Si and B–Cu@Si with low activation energy barriers of 0.54 and 0.53 eV. The moderately strong CHO* and CO* adsorption on homo-B–B@Si makes the C–C coupling viable at room temperature. Meanwhile, the feasibility trend of hetero-B–TM@Si for this coupling is observed in decreasing order: B–Cu@Si > B–Ni@Si > B–Co@Si due to the higher engagement of TM into the synergistic effect with B for increased C-affinity (CHO*) accompanied by the stronger affinity of TM with CO*. The fine-tuned electronic structure of B–Cu@Si strikes a balance between the least sluggish C(CHO*) and the most mobile CO* and promotes the coupling on B–Cu@Si. The TM dopant thereby acts as an electronic modulator for the hybrid B–TM active sites and serves as a transient site for initial CO* adsorption before participating in the coupling process. Crucially, silicene is an excellent substrate not only for stable accommodation of dopants but also for furnishing binding sites (Si*) that stabilize adsorbates, enhance C–C coupling and protect the C–O bond for the formation of ethanol. Our results pave the way for advancing a class of BACs featuring outstanding synergistic multi-active sites and illuminate mechanistic origins of CO_2RR/CORR enhancement towards high C_2 selectivity.

Data availability

The data supporting this article have been included as part of the Supplementary Information.

Author contributions

Huong T. D. Bui: conceptualization, data curation, formal analysis, methodology, investigation, and writing. Tore Brinck: conceptualization, methodology, investigation, and writing.

Conflicts of interest

There are no conflicts to declare.

Acknowledgements

This work was supported by the Swedish Research Council (VR) grant number 2021-05881. The computations were enabled by resources provided by the National Academic Infrastructure for Supercomputing in Sweden (NAISS) at the National Supercomputer Centre in Linköping University (NSC) and the PDC Centre for High Performance Computing (PDC-HPC) partially funded by the Swedish Research Council through grant agreement no. 2022-06725.

References

1 N. S. Lewis and D. G. Nocera, *Proc. Natl. Acad. Sci. U. S. A.*, 2006, **103**, 15729–15735.
2 S. Chu, Y. Cui and N. Liu, *Nat. Mater.*, 2017, **16**, 16–22.
3 A. Bagger, L. Arnarson, M. H. Hansen, E. Spohr and J. Rossmeisl, *J. Am. Chem. Soc.*, 2019, **141**, 1506–1514.
4 J. Cai, Q. Zhao, W.-Y. Hsu, C. Choi, Y. Liu, J. M. P. Martirez, C. Chen, J. Huang, E. A. Carter and Y. Huang, *J. Am. Chem. Soc.*, 2023, **145**, 9136–9143.
5 K. Fernández-Caso, G. Díaz-Sainz, M. Alvarez-Guerra and A. Irabien, *ACS Energy Lett.*, 2023, **8**, 1992–2024.
6 G. Marcandalli, M. C. O. Monteiro, A. Goyal and M. T. M. Koper, *Acc. Chem. Res.*, 2022, **55**, 1900–1911.
7 H. T. D. Bui, V. Q. Bui, X. Shao, A. Kumar, S.-G. Kim, H. M. Le, Y. Kawazoe and H. Lee, *J. Phys. Chem. C*, 2021, **125**, 13176–13184.
8 T. Yan, X. Chen, L. Kumari, J. Lin, M. Li, Q. Fan, H. Chi, T. J. Meyer, S. Zhang and X. Ma, *Chem. Rev.*, 2023, **123**, 10530–10583.
9 Y. Hori, in *Modern Aspects of Electrochemistry*, ed. C. G. Vayenas, R. E. White and M. E. Gamboa-Aldeco, Springer, New York, NY, 2008, pp. 89–189.
10 K. J. P. Schouten, Z. Qin, E. Pérez Gallent and M. T. M. Koper, *J. Am. Chem. Soc.*, 2012, **134**, 9864–9867.
11 E. Pérez-Gallent, G. Marcandalli, M. C. Figueiredo, F. Calle-Vallejo and M. T. M. Koper, *J. Am. Chem. Soc.*, 2017, **139**, 16412–16419.
12 M. Jouny, W. Luc and F. Jiao, *Nat. Catal.*, 2018, **1**, 748–755.
13 B. Ruqia, G. M. Tomboc, T. Kwon, J. Kundu, J. Y. Kim, K. Lee and S.-I. Choi, *Chem Catal.*, 2022, **2**, 1961–1988.
14 M. B. Gawande, A. Goswami, F.-X. Felpin, T. Asefa, X. Huang, R. Silva, X. Zou, R. Zboril and R. S. Varma, *Chem. Rev.*, 2016, **116**, 3722–3811.
15 S. Nitopi, E. Bertheussen, S. B. Scott, X. Liu, A. K. Engstfeld, S. Horch, B. Seger, I. E. L. Stephens, K. Chan, C. Hahn, J. K. Nørskov, T. F. Jaramillo and I. Chorkendorff, *Chem. Rev.*, 2019, **119**, 7610–7672.
16 Z. Zhang, S. Chen, J. Zhu, C. Ye, Y. Mao, B. Wang, G. Zhou, L. Mai, Z. Wang, X. Liu and D. Wang, *Nano Lett.*, 2023, **23**, 2312–2320.
17 X. Zhi, Y. Jiao, Y. Zheng and S.-Z. Qiao, *Chem. Commun.*, 2021, **57**, 9526–9529.
18 Z. Li, P. Wang, X. Lyu, V. K. R. Kondapalli, S. Xiang, J. D. Jimenez, L. Ma, T. Ito, T. Zhang, J. Raj, Y. Fang, Y. Bai, J. Li, A. Serov, V. Shanov, A. I. Frenkel,

S. D. Senanayake, S. Yang, T. P. Senftle and J. Wu, *Nat. Chem. Eng.*, 2024, **1**, 159–169.
19 J. Zhang, C. Guo, S. Fang, X. Zhao, L. Li, H. Jiang, Z. Liu, Z. Fan, W. Xu, J. Xiao and M. Zhong, *Nat. Commun.*, 2023, **14**, 1298.
20 C. Zhu, A. Chen, J. Mao, G. Wu, S. Li, X. Dong, G. Li, Z. Jiang, Y. Song, W. Chen and W. Wei, *Small Struct.*, 2023, **4**, 2200328.
21 W. Xia, Y. Xie, S. Jia, S. Han, R. Qi, T. Chen, X. Xing, T. Yao, D. Zhou, X. Dong, J. Zhai, J. Li, J. He, D. Jiang, Y. Yamauchi, M. He, H. Wu and B. Han, *J. Am. Chem. Soc.*, 2023, **145**, 17253–17264.
22 Z.-H. Zhao, J.-R. Huang, P.-Q. Liao and X.-M. Chen, *J. Am. Chem. Soc.*, 2023, **145**, 26783–26790.
23 J. Zhao, J. Zhao, F. Li and Z. Chen, *J. Phys. Chem. C*, 2018, **122**, 19712–19721.
24 T. He, K. Reuter and A. Du, *J. Mater. Chem. A*, 2020, **8**, 599–606.
25 H. Liu, Q. Huang, W. An, Y. Wang, Y. Men and S. Liu, *J. Energy Chem.*, 2021, **61**, 507–516.
26 M. He, W. An, Y. Wang, Y. Men and S. Liu, *Small*, 2021, **17**, 2104445.
27 H. T. D. Bui, V. Q. Bui, S.-G. Kim, Y. Kawazoe and H. Lee, *Phys. Chem. Chem. Phys.*, 2021, **23**, 25143–25151.
28 X. Lin and J. Ni, *Phys. Rev. B: Condens. Matter Mater. Phys.*, 2012, **86**, 075440.
29 J. Feng, Y. Liu, H. Wang, J. Zhao, Q. Cai and X. Wang, *Comput. Mater. Sci.*, 2014, **87**, 218–226.
30 W. Xia, W. Hu, Z. Li and J. Yang, *Phys. Chem. Chem. Phys.*, 2014, **16**, 22495–22498.
31 S. S. Raya, A. S. Ansari and B. Shong, *Surf. Interfaces*, 2021, **24**, 101054.
32 W. Liao, G. Yu, L. Zhao, H. Zhu and W. Chen, *Nanoscale*, 2022, **14**, 10918–10928.
33 H. T. D. Bui and T. Brinck, *J. Mater. Chem. A*, 2024, **12**, 2110–2120.
34 T. Brinck and S. K. Sahoo, *Phys. Chem. Chem. Phys.*, 2023, **25**, 21006–21019.
35 G. Kresse and J. Furthmüller, *Phys. Rev. B: Condens. Matter Mater. Phys.*, 1996, **54**, 11169–11186.
36 G. Kresse and J. Furthmüller, *Comput. Mater. Sci.*, 1996, **6**, 15–50.
37 G. Kresse and J. Hafner, *Phys. Rev. B: Condens. Matter Mater. Phys.*, 1993, **47**, 558–561.
38 J. P. Perdew, K. Burke and M. Ernzerhof, *Phys. Rev. Lett.*, 1996, **77**, 3865–3868.
39 G. Kresse and D. Joubert, *Phys. Rev. B: Condens. Matter Mater. Phys.*, 1999, **59**, 1758–1775.
40 P. E. Blöchl, *Phys. Rev. B: Condens. Matter Mater. Phys.*, 1994, **50**, 17953–17979.
41 S. Grimme, J. Antony, S. Ehrlich and H. Krieg, *J. Chem. Phys.*, 2010, **132**, 154104.
42 K. Mathew, R. Sundararaman, K. Letchworth-Weaver, T. A. Arias and R. G. Hennig, *J. Chem. Phys.*, 2014, **140**, 084106.
43 W. Tang, E. Sanville and G. Henkelman, *J. Phys.: Condens. Matter*, 2009, **21**, 084204.
44 S. Maintz, V. L. Deringer, A. L. Tchougréeff and R. Dronskowski, *J. Comput. Chem.*, 2016, **37**, 1030–1035.
45 V. Wang, N. Xu, J.-C. Liu, G. Tang and W.-T. Geng, *Comput. Phys. Commun.*, 2021, **267**, 108033.
46 D. M. Bylander and L. Kleinman, *Phys. Rev. B: Condens. Matter Mater. Phys.*, 1992, **46**, 13756–13761.
47 G. Henkelman, B. P. Uberuaga and H. Jónsson, *J. Chem. Phys.*, 2000, **113**, 9901–9904.
48 A. V. Krukau, O. A. Vydrov, A. F. Izmaylov and G. E. Scuseria, *J. Chem. Phys.*, 2006, **125**, 224106.
49 S. Lebègue and O. Eriksson, *Phys. Rev. B: Condens. Matter Mater. Phys.*, 2009, **79**, 115409.
50 J. C. Garcia, D. B. de Lima, L. V. C. Assali and J. F. Justo, *J. Phys. Chem. C*, 2011, **115**, 13242–13246.
51 S. Cahangirov, M. Topsakal, E. Aktürk, H. Şahin and S. Ciraci, *Phys. Rev. Lett.*, 2009, **102**, 236804.
52 A. J. Garza, A. T. Bell and M. Head-Gordon, *ACS Catal.*, 2018, **8**, 1490–1499.
53 T. K. Todorova, M. W. Schreiber and M. Fontecave, *ACS Catal.*, 2020, **10**, 1754–1768.
54 Y. Zhou, F. Che, M. Liu, C. Zou, Z. Liang, P. De Luna, H. Yuan, J. Li, Z. Wang, H. Xie, H. Li, P. Chen, E. Bladt, R. Quintero-Bermudez, T.-K. Sham, S. Bals, J. Hofkens, D. Sinton, G. Chen and E. H. Sargent, *Nat. Chem.*, 2018, **10**, 974–980.
55 J. H. Montoya, A. A. Peterson and J. K. Nørskov, *ChemCatChem*, 2013, **5**, 737–742.
56 J. K. Nørskov, F. Studt, F. Abild-Pedersen and T. Bligaard, *Fundamental Concepts in Heterogeneous Catalysis*, John Wiley & Sons, Ltd, 1st edn, 2014.